UCLA

Title
Intraocular robotic interventional surgical system (IRISS): Semi-automated OCT-guided cataract removal.

Permalink

Journal

ISSN

Authors
Chen, Cheng-Wei
Chen, Cheng-Wei
Lee, Yu-Hsiu
et al.

Publication Date

DOI

Intraocular Robotic Interventional Surgical System (IRISS): Semi-Automated OCT-Guided Cataract Removal

Cheng-Wei Chen, Yu-Hsiu Lee, Matthew J. Gerber, Harrison Cheng, Yan-Chao Yang,
Andrea Govetto, Anibal Andrés Francone, Stefano Soatto, Warren S. Grundfest, Jean-Pierre Hubschman, and
Tsu-Chin Tsao

Abstract—*Background:* **With the development of laser-assisted platforms, the outcomes of cataract surgery have been improved by automating several procedures. The cataract-extraction step continues to be manually performed, but due to deficiencies in sensing capabilities, surgical complications such as posterior capsule rupture and incomplete cataract removal remain.**

Methods: **An optical coherence tomography (OCT) system is integrated into our IRISS robot. The OCT images are used for preoperative planning and intraoperative intervention in a series of automated procedures. Real-time intervention allows surgeons to evaluate the progress and override the operation.**

Results: **The developed system was validated by performing lens extraction on 30 post-mortem pig eyes. Complete lens extraction was achieved on 25 eyes and "almost complete" extraction was achieved on the remainder due to an inability to image small lens particles behind the iris. No capsule rupture was found.**

Conclusions: **The IRISS successfully demonstrated semi-automated OCT-guided lens removal with real-time supervision and intervention.**

Keywords—**robot-assisted ophthalmic surgery, OCT-guided surgery, robotic surgery, intraocular surgery, automated cataract surgery, cataract extraction**

I. BACKGROUND AND MOTIVATION

Cataracts—an opaque clouding of the lens in the eye—are the leading cause of blindness in the world [1]. Cataract-induced blindness is remedied by cataract surgery, which is the most frequently performed surgical procedure in the United States [2]. With a success rate over 90%, cataract surgery represents one of the most successful intraocular procedures [3]. However, due to the physiological limitations of a human surgeon and deficiencies in sensing capabilities, surgical complications remain, including posterior capsule rupture (1.8–4.4%), incomplete lens removal (1.1%), and corneal incision leakage (1.2%) [4]. To improve surgical outcomes, it is necessary to improve the visualization of anatomical features inside the eye and to use that information to safely and efficiently guide a surgical instrument.

To visualize intraocular tissues, non-invasive imaging technologies such as magnetic resonance imaging, ultrasound biometry, and optical coherence tomography (OCT) have been developed and used in preoperative and postoperative diagnoses. Magnetic resonance imaging provides high-contrast and high-resolution images [5] but is unsuitable for intraoperative surgical procedures due to physical space constraints, high field strengths, and low frame rates. High-frequency ultrasound biometry provides real-time, high-

resolution images [6] but requires a contact medium between the probe and the eye to reduce signal reflection. In contrast, OCT provides a non-contact, real-time, high-resolution imaging modality that can be integrated into surgical instruments and microscopes [7], [8]. Most importantly, it has been shown that intraocular tissues can be visualized in OCT scans in both anterior [9] and posterior segments [10].

Cataract surgery (refer to Fig. 1) involves a suite of procedural steps including (1) creating a corneal incision, (2) removing the anterior capsule via capsulorhexis, (3) fragmenting the cataract into pieces of lens material, (4) emulsifying and aspirating the lens material using an ultrasonic surgical instrument, (5) aspirating the remaining lens material with an irrigation-aspiration (I/A) tool, and (6) inserting an intraocular lens implant. The first three steps (corneal incision, capsulorhexis, and fragmentation) have been partially or fully automated by OCT-based femtosecond laser systems [11]–[15]. Automation of the final step (implant insertion) has also been investigated to improve precision over that of a human surgeon [16]. However, the cataract-extraction procedure remains a manually performed operation, despite being the main source of the aforementioned surgical complications.

Even if provided with the "best" visual feedback, a surgeon cannot perform surgical procedures absolutely accurately unless the physiological limitations of tactile control are overcome. To address the stringent requirements of intricate tool manipulation, robot-assisted surgical platforms have been investigated by several groups. Johns Hopkins University developed a steady-hand manipulator for membrane peeling [17]. The University of Tokyo demonstrated the feasibility of a robotic system in performing vitreoretinal tasks such as posterior vitreous detachment, vessel sheathotomy, and microcannulation [18], [19]. Vanderbilt University demonstrated robotic capabilities of conducting constrained ocular manipulation, membrane peeling, and stent deployment [20]. The University of Utah designed a compact, remotely operated manipulator for disposable instruments and performed membrane peeling on an eye phantom [21]. The University of Munich tested the efficacy of a target-based injection platform on pig eyes aimed at assisting the treatment of age-related macular degeneration [22]. In our previous work, the IRISS successfully demonstrated the feasibility of remotely operated cataract surgery and vein cannulation via mechanism design and motion filtering [23].

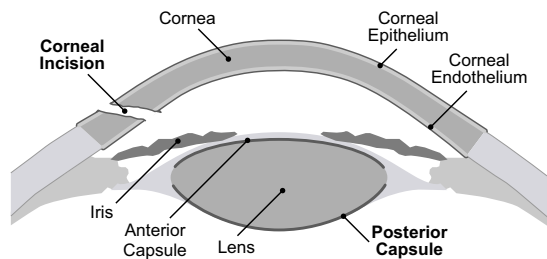Recognizing the advantages of integrating high-resolution

Fig. 1: Shown is a schematic of the anterior segment with relevant features labeled. Both the posterior capsule and the corneal incision are important features and are repeatedly referred to throughout this paper.

OCT imaging with a high-precision robotic platform, several groups have demonstrated success in robot-assisted intraocular surgical intervention using OCT. A team from the Cleveland Clinic integrated an OCT probe with a surgical microscope to provide high-resolution visual feedback [24]. More recently, the same group proposed using a stereo-tracked i-OCT system to automatically deploy scans in real-time near the surgical instrument tip to ease the effort of probe re-allocation [25]. Vanderbilt University integrated an OCT fiber optic cable into the tool and conducted epiretinal membrane peeling using a master-slave configuration guided by OCT B-scans [26]. The same team also demonstrated a semi-automated micro-injection via the assistance of three-dimensional virtual fixtures based on both microscope and B-mode OCT feedback [27]. Johns Hopkins University incorporated an A-mode OCT as a distal sensor with a piezo-motor in the hand-held tool piece to achieve active depth-locking control [28]. The depth-locking feature was applied to the OCT-embedded micro-forceps for epiretinal membranectomy [29].

Despite the advances in both robotic platforms and OCT-based technologies, several unresolved issues remain, particularly in the case of cataract extraction. First, the location where a surgical instrument passes through the cornea (the "corneal incision") must be constrained throughout surgery to decrease undesirable trauma in adjacent corneal tissue. However, the methods in existing work to align the remote center of motion (RCM) of the robot to the corneal incision are contact-based and require well-calibrated kinematics. In addition, no methods exist to automate the procedure or to guarantee successful alignment and insertion. Second, despite the wealth of anatomical information provided by OCT-based systems, no existing work uses OCT scans to reconstruct the surgical environment for trajectory planning of the surgical instrument or for automation of the surgical procedures. Third, the surgical information acquired from real-time OCT A or B modes used in previous work [27], [29] is noisy and insufficient to represent the constantly changing intraocular environment. In other words, an automated surgical platform must be capable of adapting, in real-time, to the dynamic nature of its surgical workspace.

This work addresses these concerns by developing and implementing an OCT-guided robotic platform. The main contributions are:

1) An automated procedure that extracts information from an OCT scan to align the RCM of the robot to the corneal incision. In contrast to existing methods, this procedure enables the minimization of physical stress in corneal tissue during surgical operations.
2) A method that uses OCT scans to generate a three-dimensional parameterized model of the anatomical eye structure with safe surgical zones of operation.
3) A method to use the eye model to plan a safe, efficient tool-tip trajectory through the workspace. This method has the advantage of preventing tissue damage and posterior capsule rupture by reducing the risk of inadvertent collision between the instrument and tissues.
4) The development of intraoperative diagnostics and intervention methods to allow the surgeon to override or modify any portion of the automated cataract-extraction procedure, including tool-tip trajectory and the predefined workspace. This functionality serves to improve the flexibility and safety of the automation in the event of unexpected disturbances.

These contributions were experimentally validated by performing lens extraction on 30 post-mortem pig eyes.

This paper is organized as follows. Section II provides a system overview and introduces the integrated components of the OCT-guided robotic platform. Section III describes the entire cataract-extraction process using the OCT-guided robotic platform. Section IV presents the evaluation of the system and the experimental results on post-mortem pig eyes.

II. System Overview

The system architecture of the OCT-guided robotic system is shown in Fig. 2. The IRISS controls both the I/A tool-tip position and the irrigation and aspiration forces generated by the Alcon ACCURUS system [30]. The I/A tool-tip position is programmed based on the anatomical model reconstructed from OCT volume scans, which are obtained from the OCT probe positioned over the eye (Fig. 3). The OCT and embedded camera provide real-time visual feedback to the surgeon. The surgeon can override the IRISS during automated operation to assess surgical progress and to account for variations in the surgical environment.
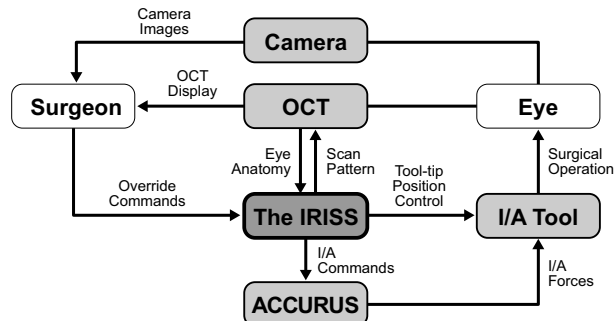

Fig. 2: Shown is the overall system architecture for the OCT-guided robotic system. See Supplemental Video 1 for details.
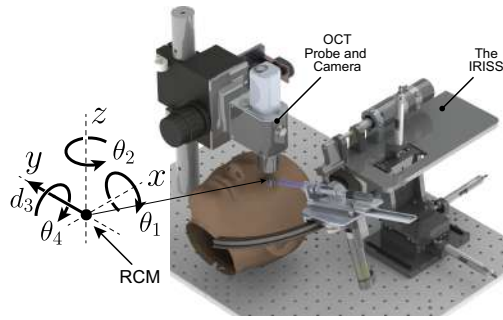
Fig. 3: Shown is a CAD model of the integrated system with the coordinate frame and kinematic variables defined. See Supplemental Video 2 for system integration details.

A. The IRISS

The IRISS consists of two, independently controllable manipulator arms, each holding two interchangeable surgical instruments [23]. However, lens extraction (on pig eyes) only requires a single I/A tool and therefore only one manipulator arm is used in this study. The I/A tool is mounted to a carriage that rides on a circular track which is rotated about a shaft mounted to the base of the IRISS. This spherical mechanism kinematically guarantees a mechanically fixed RCM. To allow three-dimensional translation of the RCM relative to the eye, the arm assembly is mounted to a motorized linear stage capable of three-dimensional XYZ translation. Details of the mechanical design of the IRISS and an evaluation of its performance can be found in [23].

For convenient mathematical representation, the Cartesian coordinate frame of the IRISS is chosen to be coincident with the RCM (Fig. 3). Tool-tip positions are achieved by the coordination of two rotational angles (θ_1 and θ_2) and one translational displacement (d_3). Kinematically, the tool rotation about its centerline (θ_4) has no effect on tool-tip position. Prior to surgery, mechanical calibration is performed to ensure the commands $\theta_1 = \theta_2 = \theta_4 = 0$ and $d_3 = 0$ correspond to a configuration in which the tool tip is located coincident with the RCM and the aspiration port facing anterior. Given a tool-tip position $\boldsymbol{p} = [p_x \; p_y \; p_z]^{\mathsf{T}}$ inside the eye, the inverse kinematics are given by

$$\begin{cases} \theta_1 = \text{atan2}\left(-p_z, \; p_y\right) \\ \theta_2 = \text{atan2}\left(-p_x, \; \sqrt{p_y^2 + p_z^2}\right) \\ d_3 = \|\boldsymbol{p}\|_2 \end{cases} \tag{1}$$

where $\text{atan2}(\cdot, \cdot)$ is the four-quadrant inverse tangent function with two arguments and $\|\cdot\|_2$ is the Euclidean norm.

For the duration of the cataract-extraction procedure, the tool tip remains inside the eye and Eqn. 1 defines a unique map from the tool-tip position to the robotic joint space. However, when the tool tip is outside the eye, motion control is realized in joint space and the kinematic singularity at $[0 \; 0 \; 0]^{\mathsf{T}}$ (the RCM) is avoided. Doing so has the advantage of directly coupling the desired insertion angles to joint angle commands (Section III-A).

B. The OCT System

A commercially available ThorLabs SD-OCT imaging system (Telesto II 1060LR) is integrated with the IRISS (Fig. 3). The OCT system operates with a broadband superluminescent diode with a central wavelength of 1060 nm, axial resolution of 9.18 μm, and imaging depth in air of 9.4 mm. The objective lens (LSM04BB) exhibits a focal length of 54 mm, a lateral resolution of 25 μm, and a 10×10 mm field of view. The OCT probe has been vertically actuated with a translational stage for changing its depth of view.

The integrated OCT system is capable of performing three-dimensional volume scans, real-time A-scans and B-scans, and custom scanning patterns programmed through the provided software development kit. Volume scans are used for automated alignment (Section III-A), modeling of anatomical structure (Section III-B), and intermittent assessment (Section III-D). Real-time B-scans and custom scanning patterns are used for real-time intraoperative intervention (Section III-D). Although it is common for anterior-segment OCT to use a laser with central wavelength of 1310 nm to penetrate tissue to a greater depth [9], this system uses an illumination source with central wavelength of 1060 nm as a balance between signal attenuation and imaging depth. To image the anterior segment of pig eyes (which have a thicker lens than that of humans [31]), tissue penetration is sacrificed in favor of signal transmittance by shortening the wavelength of the illumination source.

C. System Integration

The hardware integration architecture is shown in Fig. 4. The IRISS is controlled by a National Instruments PXI real-time target at a sampling rate of 1 kHz. Brushed DC motors on the IRISS joints are driven by current-type amplifiers. The control loops are closed by rotary optical encoders integrated into the motors. Aspiration and irrigation functions are realized by integrating the ACCURUS with the IRISS. The ACCURUS provides integrated functions for intraocular surgery. In cataract surgery, it enables fluid aspiration and irrigation through the I/A tool. The vacuum force applied to aspiration was originally controlled with a foot pedal connected to the ACCURUS machine. In this study, the I/A commands are sent from the NI PXI to the ACCURUS by emulating the foot pedal's analog communication protocol.

The joint motions to the IRISS and the I/A commands to the ACCURUS either follow a trajectory provided by the trajectory planner (Section III-C) or are directly controlled by user command. The host PC acquires OCT scans and camera images from the OCT system, which is driven by a base unit that positions its A-scans. The host PC runs with a graphical user interface programmed in LabVIEW. Through this interface, the user can supervise real-time scanning of the workspace, and—if necessary—override the tool-tip trajectory or the I/A commands (Section III-D).

To enable control of the IRISS using OCT feedback, the registration between the OCT reference frame and the IRISS frame was required. To derive this relationship, the IRISS was autonomously commanded to touch a series of points
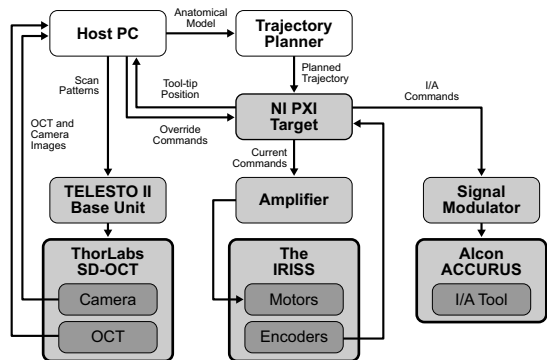
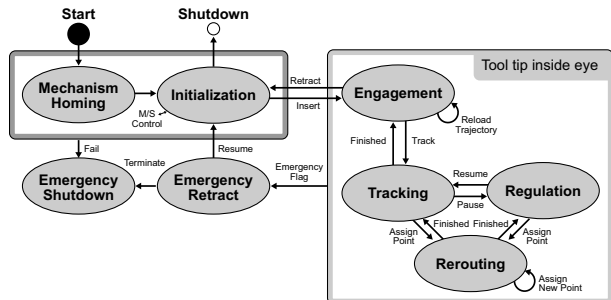Fig. 4: Shown is a diagram of the hardware architecture.

Fig. 5: Shown is the software state chart for the OCT-guided surgical robotic system.

that formed a unique, non-symmetric pattern representational of the intraocular workspace. At each point, the tool-tip position was determined in the OCT frame from medium-sensitivity (48 kHz) volume scans by applying a custom, image-processing algorithm as follows. In each B-scan slice of the medium-sensitivity volume scan, the 2D matrix of raw data is converted to a binary image by an intensity scaling that allows for application of a constant binary threshold. After noise removal, the remaining points in the binary slice are converted to Cartesian coordinates in the OCT frame and added to a 3D point cloud. A cylinder is fit to this point cloud, which represents the physical tool and its centerline. To find the tool tip, the transition between a B-scan slice with a visible tool and one without a visible tool is considered to be the location of the tool tip. The intersection of the found tool centerline with this slice is the tool tip location.

At each point the IRISS was commanded to touch, two representations existed: the tool-tip position in the IRISS frame from the ideal forward kinematics and the tool-tip position in the OCT frame from the volume scan. Procrustes superimposition was performed to find the linear transformations (translation, rotation, and uniform scaling) between the frames [32]. With the linear transformations and their inverses known, any point in the OCT reference frame can be converted to a point in the IRISS reference frame—and vice versa. This initial registration is dynamically updated in real-time when the IRISS or the OCT probe are moved, thereby maintaining the validity of the registration despite the relative motion between the hardware components.

D. Software Design

The software state chart is shown in Fig. 5. In the mechanism homing state, each joint is incrementally actuated until its homed position is found via a photo-interrupter sensor. In the initialization state, the I/A tool is commanded to a safe, predefined initial position and the RCM of the IRISS is automatically aligned to the corneal incision in the eye (Section III-A). Then, the I/A tool is inserted into the eye, a surgical trajectory is loaded into the software, and the tool begins tracking the predefined cataract-extraction trajectory (Section III-C). During the tracking, the user may pause the motion or reroute the tool tip to a specific point. The tracking process is considered complete when either the end of the trajectory has been reached or a finishing command has been sent from the user. At this point, the tool returns to the engaged state to await tool retraction or additional track commands.

For safety reasons, emergency retraction and shutdown are included in the state chart. For example, in the event of homing sensor malfunction, the program will terminate to prevent hardware damage. On the other hand, emergency tool retraction is employed in the states where the tool tip is within the eye. To prevent surgical damage that would occur during emergency shutdown if the tool remained inside the eye, the system is powered off only when the tool is fully retracted and any existing operations have been terminated.

III. AUTONOMOUS CATARACT EXTRACTION

The core contribution of this work is the proposed methodology for autonomous cataract extraction. This methodology can be divided into four distinct steps: automated alignment and tool insertion (Section III-A), segmentation and modeling of anatomical structures (Section III-B), preoperative trajectory planning (Section III-C), and cataract extraction with intraoperative intervention (Section III-D).

A. Automated Alignment and Tool Insertion

The first step of autonomous cataract extraction involves aligning the OCT probe and the IRISS to the eye such that (1) the OCT probe is optimally positioned to intraoperatively image the eye, (2) the tool tip remains within the OCT scanning volume for the duration of the cataract-extraction procedure, and (3) the mechanical RCM of the robot is coincident with an approximation of the corneal incision, a point p^*_{CI}. Proper alignment and subsequent tool insertion rely on characterizing the corneal incision from an OCT volume scan.

Using visual servoing with the embedded camera as feedback, the OCT stage is translated until the optical center of the pupil is coincident with the optical center of the camera. This position is optimal for imaging the lens during cataract extraction, but for any typical pig eye, the corneal incision is outside the OCT scanning range when the stage is in this position.. Therefore, displacement data from previous experiments are used to translate the OCT probe over the expected location of the corneal incision and to an appropriate scanning depth. Any resulting positional

error is inconsequential because a typical corneal incision (approximate corneal epithelium arc length 2–3 mm) easily fits within the OCT scan boundary (dimensions 10×10 mm).

An automated algorithm is run on an acquired high-sensitivity (5.5 kHz) volume scan of the corneal incision. In each B-scan slice, the cornea incision appears as a high-intensity line segmenting the cornea. This line can be detected through a Hough transform and its two intersection points with the epithelium and endothelium are recorded to form a 3D point cloud. These points are shown as the dark points in Fig. 7. The average point of each set (epithelium and endothelium) determines the endpoints of a line that passes through the corneal incision (shown as the solid line in Fig. 7). From this line, and the epithelium and endothelium set of points, three sets of information are obtained: (1) The corneal incision characterized by its depth, its angle with respect to the optical equator, and the epithelium and endothelium arc lengths. These metrics are useful for assessing the surgical "quality" of the incision and for postoperative evaluation. (2) A point $\boldsymbol{p}_{CI}^*$ defined to best approximate the location of the corneal incision in the IRISS frame (Fig. 6). (3) A pair of tool-insertion angles, θ_1^* and θ_2^*, allows the tool to pass through the corneal incision determined by the incision angle with respect to the optical equator.

Together, $\boldsymbol{p}_{CI}^*$, θ_1^*, and θ_2^* define an optimal insertion trajectory (red line in Fig. 6) for inserting the tool in a single, fully automated step with minimal resulting stress to the cornea. The output of this algorithm is shown in Fig. 7.

With $\boldsymbol{p}_{CI}^*$ known, aligning the mechanical RCM to the corneal incision is trivial. The tool is commanded to a safe, retracted position ($\theta_1 = \theta_2 = \theta_4 = 0$ and $d_3 = -30$ mm) and the XYZ stage is commanded such that the mechanical RCM is coincident with $\boldsymbol{p}_{CI}^*$. This aligns the IRISS to the eye.

For automated tool insertion, the IRISS is commanded to the calculated insertion angles ($\theta_1 = \theta_1^*$ and $\theta_2 = \theta_2^*$) and the tool is moved such that its tip is just outside the corneal incision ($d_3 = -0.5$ mm). At this point, all motion is automatically paused and the tool-tip position and tool pose can be assessed by the surgeon. If unacceptable, manual input can override the joint angles and RCM position. If acceptable, automated insertion is initiated. During insertion, the tool-tip velocity and irrigation are functions of the surrounding tissue: once the corneal epithelium is crossed, the velocity is decreased and irrigation is initiated. The slower velocity
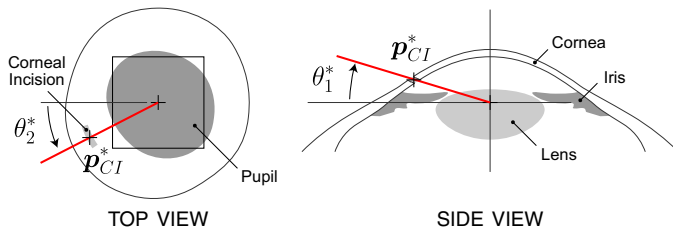

Fig. 6: Shown is a schematic of the insertion angles and approximate corneal incision point. The red line indicates the calculated insertion trajectory.
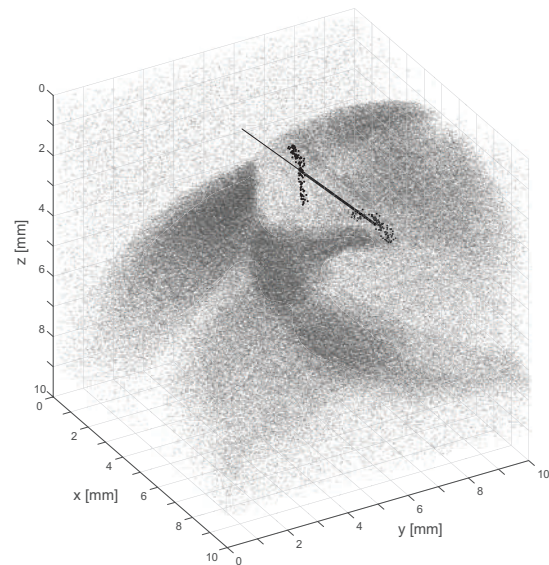

Fig. 7: Shown is an output plot of the algorithm to detect the corneal incision. Raw OCT data is represented as the point cloud, the darker points represent detected incision points on the epithelium and endothelium, and the calculated insertion trajectory through the corneal incision is shown as the solid line. Calculated metrics (in the IRISS frame) were $\theta_1^* = 60.54°$, $\theta_2^* = 5.89°$, and $\boldsymbol{p}_{CI}^* = [1.78\ 0.64\ -0.02]^\mathsf{T}$.

prevents corneal leakage and the active irrigation maintains intraocular pressure and prevents corneal collapse. Insertion is considered complete at $d_3 = 2$ mm.

B. Segmentation and Modeling of Anatomical Structure

To account for anatomical variation between eyes, a pair of preoperative OCT volume scans are acquired of the anterior segment. Because the depth of the posterior capsule (approximately 10–15 mm from the top of the cornea) is greater than the sensing range of the OCT (9.4 mm), the OCT probe is physically translated via its translational stage to cover the entire range of interest. Two scans are sufficient: a representative B-scan of the upper portion is shown in Fig. 8a and includes the iris and cornea; a representative B-scan of the lower portion is shown in Fig. 8b and includes the posterior capsule and the inverted iris. The iris appears inverted in the lower scan due to the limited sensing depth of the OCT system. To avoid overlapping the posterior capsule with the inverted iris, the lower scan is taken when the posterior capsule appears (by visual inspection) within the top 3 mm of the OCT frame and the inverted iris is located in the bottom 5 mm (Fig. 8b).

After acquisition, the two scans are stitched together with the known displacement of the OCT probe to create a single, composite scan of the entire anterior segment. The volume scan data are converted to a point cloud by automated binary thresholding (a consistent grey-level threshold value is applied after normalization of the intensity of every each B-scan slice). The point cloud represents tissue whose reflection is stronger than that of water or balanced salt solution and is therefore a down-sampled representation of anatomical features of interest. For tool-tip navigation within the eye,
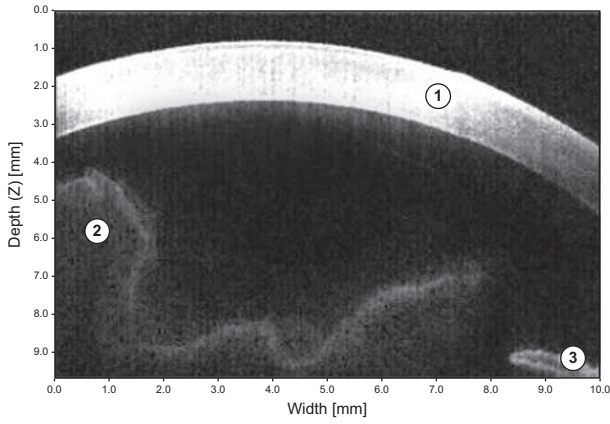
(a) Shown is an OCT scan of the upper anterior segment including (1) the cornea, (2) lens material, and (3) the iris.
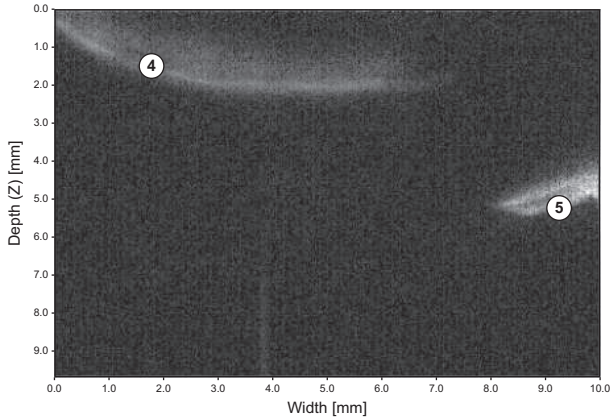
(b) Shown is an OCT scan of the lower anterior segment including (4) the lens and posterior capsule and (5) the inverted iris.
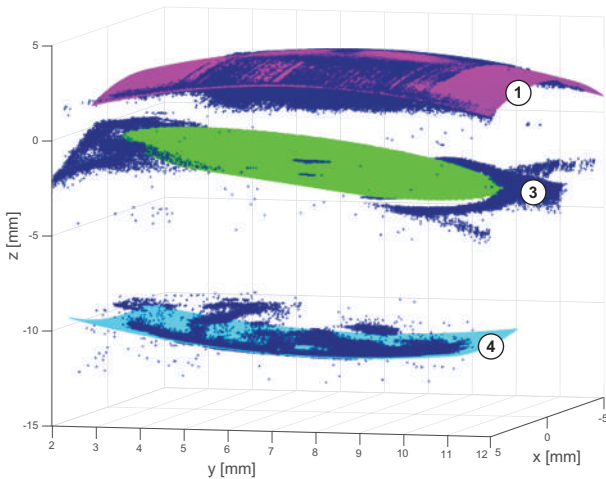
(c) Shown is the reconstructed eye model. (1) Magenta: reconstructed cornea, (3) green: reconstructed pupil, (4) cyan: reconstructed posterior capsule, blue points: raw OCT data.

Fig. 8: OCT-based modeling of eye anatomy.

it is critical to determine the positions of the cornea, iris, and posterior capsule from this point cloud data.

Although various approaches exist for OCT image segmentation of anterior structures, all require significant computational resources to produce accurate results [33]. If

implemented, the surgical consequence would be a protracted delay prior to the start of surgical procedures, during which the cornea will begin to collapse. Therefore, a custom algorithm was developed that considers *a priori* knowledge of the eye anatomy to quickly generate (within 1 minute) a parameterized anatomical model with acceptable accuracy (≤ 100 µm). The pupil was modeled as a 2D ellipse in 3D space. For segmentation of the cornea, a second-order parabolic surface was chosen to represent the corneal epithelium and was fit to the point-cloud data using a least-squares method. This fit uses the knowledge that the cornea must be located near the top of the scan volume. Similarly, for segmentation of the posterior capsule, a second-order parabolic surface was chosen.

The reconstructed cornea, pupil, and posterior capsule defines the workspace within the anterior segment (Fig. 8c). This model is parameterized and is used to preoperatively plan the cataract-extraction trajectory. Due to the effective range of the I/A tool aspiration, a safety margin around all three anatomical features was enforced in the model. This guaranteed that any composite error from the segmentation and modeling was alleviated for errors less than this margin.

It is important to note that the medium through which the OCT laser signal propagates is variable. Specifically, when the laser signal passes from air into the corneal epithelium, the refractive index changes from 1 to approximately 1.35 (that of water). For this reason, the depth values acquired from the OCT system, z_o, are adjusted to update the anatomical model to account for this change:

$$z_o' = \begin{cases} z_o, & z_o < z_e \\ z_e + n\,(z_o - z_e), & z_o \geq z_e \end{cases} \quad (2)$$

where z_o' is the adjusted depth value, z_e is the depth of the corneal epithelium along an A-scan line, and n is the ratio of the refractive index of air over that of water ($n \approx 0.74$).

C. Preoperative Trajectory Planning

In this step, a tool-tip trajectory for cataract extraction is generated based on the eye model obtained in the previous step, allowing the IRISS to guide the I/A tool with respect to anatomical structures within the eye. The generated tool-tip trajectory exhibits the following characteristics:

(i) The geometry of the trajectory is chosen to mobilize the lens material and to increase surgical efficacy and efficiency.

(ii) The tool-tip motion deepens and decelerates after each repetition of a baseline trajectory to avoid posterior capsule rupture.

(iii) The aspiration and θ_4 are scheduled as functions of the tool-tip position to increase surgical efficacy and provide protection against posterior capsule rupture.

(1) Trajectory Pattern Design: Based on surgeon input and clinical feedback, a flower-shaped pattern with a scooping motion was developed (Fig. 9 and 10). The geometric shape in the plane of the pupil is intended to disaggregate conglomerated lens material, while the scooping motion is intended
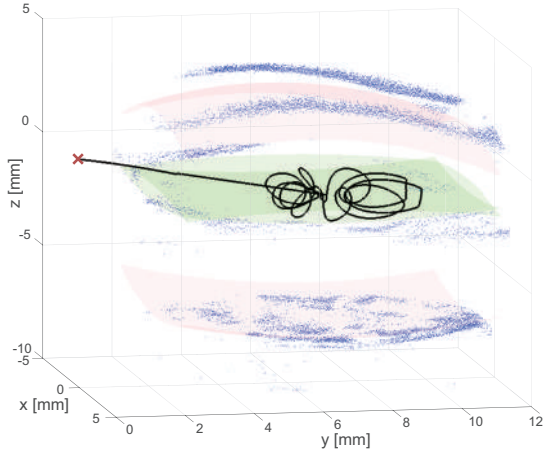
Fig. 9: Shown is the preoperatively planned cataract-extraction trajectory in the IRISS frame. Point cloud: raw OCT data, solid black line: tool-tip trajectory, red surfaces: safety margins, green surfaces: tool-tip workspace, red X: the RCM.
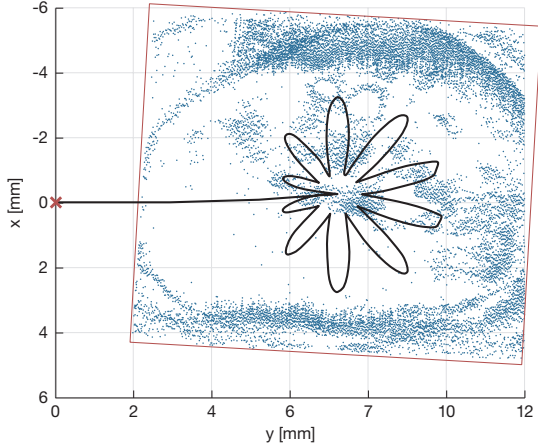

Fig. 10: Shown is the top view of Fig. 9. Point cloud: raw OCT data, solid black line: tool-tip trajectory, red X: the RCM, red box: OCT scanning volume.

to detach lens material from the posterior capsule. Given a desired tool-tip trajectory, $\boldsymbol{p}(t) = [p_x(t) \; p_y(t) \; p_z(t)]^{\mathsf{T}}$, then

$$\begin{cases} p_x(t) = c_x + q\cos(\theta(t)) \\ p_y(t) = c_y + q\sin(\theta(t)) \\ p_z(t) = c_z - wa\sin(n\theta(t)) \end{cases} \quad (3)$$

where $\boldsymbol{c} = [c_x \; c_y \; c_z]^{\mathsf{T}}$ is the coordinate of the iris center, a is a position-dependent amplitude bounded by the distances to the anterior and posterior capsular surfaces, n is the number of "flower petals" in the geometric pattern, and q is the two-dimensional motion of the tool tip in polar coordinates defined as:

$$q(t) = (sR - wr)\sin^2\left(\frac{n\theta(t)}{2}\right) + wr \quad (4)$$

where s is the radial scaling of the flower pattern, R is the pupil radius, r is the inner radius of the flower pattern, w is a window function between $[0,1]$ such that the trajectory will start and end at $\boldsymbol{c}$, and $\theta(t)$ is the angle between the x-axis
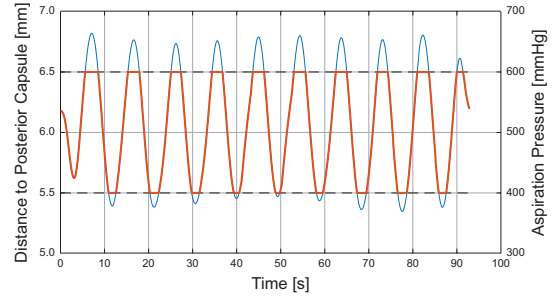

Fig. 11: Shown is an example of an aspiration force profile scheduled along the tool-tip trajectory with $z_{lb} = 5.5$ mm, $z_{ub} = 6.5$ mm, $f_{a,lb} = 400$ mmHg, and $f_{a,ub} = 600$ mmHg.

and a line from $\boldsymbol{c}$ to the tool tip in the range $[0, 2\pi]$. The value of $\theta(t)$ was chosen with equidistant sampling in polar coordinates with an approximately averaged tool-tip velocity of 0.6 mm/s and cycle time of 90 s.

Based on clinical experience, it is necessary to move the tool slower and deeper after each cycle to detach and aspirate lens material. Therefore, the tool moves fastest for the first cycle (approximately averaged tool-tip velocity: 0.6 mm/s) and at a conservative, shallow depth (within the top 30% of the capsular bag thickness). Each subsequent cycle progresses the tool tip deeper ($+10\%$ lens thickness per cycle) and slower (-25% tool-tip velocity).

(2) Instrument Rotation: The aspiration port of the I/A tool is located on the side of the instrument near its tip. Posterior capsule rupture may occur when the port aspirates the capsular surface in close proximity. For this reason, θ_4 is scheduled with the aspiration port always facing away from the posterior capsule. Also, when the tool tip is near the equator of the capsular bag, the normal vector of the port is directed towards a virtual axis above the iris center $\boldsymbol{c}$,

$$\{(x, y, z) \in \mathbb{R}^3 : x = c_x \text{ and } z = c_z + \Delta z_a\} \quad (5)$$

where $\Delta z_a > 0$ indicates the offset between the iris center and the virtual axis. The position-dependent instrument rotation can be described as:

$$\theta_4(t) = \text{atan2}\left(p_x - c_x, \; p_z - c_z - \Delta z_a\right) \quad (6)$$

(3) Aspiration Force Scheduling: Even if the aspiration direction is accounted for, posterior capsule rupture may still occur if the aspiration magnitude is ignored. Therefore, the aspiration is also scheduled based on $\Delta z_p(t)$, the distance between the tool tip and the posterior capsule (Fig. 11). This is achieved by the following position-dependent aspiration scheduling:

$$f_a(t) = f_{a,lb} + (f_{a,ub} - f_{a,lb})\,\text{sat}\left[\frac{\Delta z_p(t) - z_{lb}}{z_{ub} - z_{lb}}\right] \quad (7)$$

where $f_a(t)$ is the aspiration force as a function of tool-tip position; $(\cdot)_{lb}$ and $(\cdot)_{ub}$ are shorthand notations for the lower and upper bounds of a parameter; $\text{sat}(\cdot)$ is the saturation function with both domain and co-domain $[0,1]$; and z_{lb} and z_{ub} are user-defined bounds on the magnitude of $\Delta z_p(t)$.

This saturation is necessary to provide sufficient force for aspiration without becoming too aggressive and deforming the intraocular tissue.

Once the cataract-extraction trajectory is generated, a top view of the calculated tool-tip trajectory is projected on an anterior view of the eye in the graphical user interface. Likewise, the side view of the calculated tool-tip trajectory is projected on a superior view of the eye. If any adjustment is requested by the surgeon, offsets and range resizing can be manually performed.

D. User Interface for Intraoperative Intervention

Automated cataract extraction is conducted by tracking the predefined trajectory and scheduling the aspiration. However, while the preoperative scan is useful in constructing an initial anatomical model and tool trajectory, the intraoperative anterior segment is a dynamic environment subject to change during surgical operations. To account for the variable surgical environment, intraoperative supervision and manual intervention strategies are provided to the surgeon during the autonomous cataract-extraction procedure.

1) Real-Time OCT Assessment: During automated tracking, either OCT B-scans (Fig. 12) or localized B-scans that intersect and track the tool tip (Fig. 13) are displayed to the user in real-time for monitoring surgical progress. Both
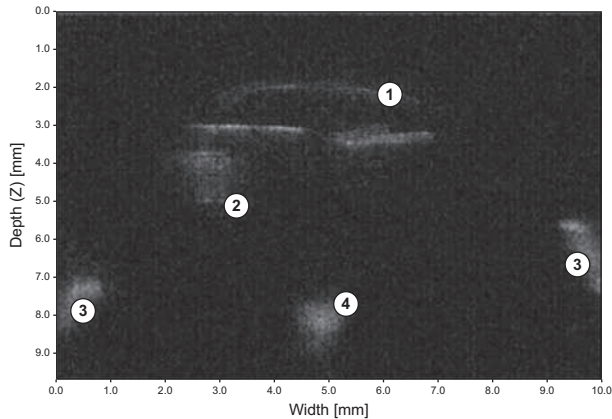

Fig. 12: Shown is an example of the real-time OCT image feedback. Visible features are (1) the posterior capsule, (2) lens material, (3) the iris, and (4) the tool tip. Note: all images are inverted.
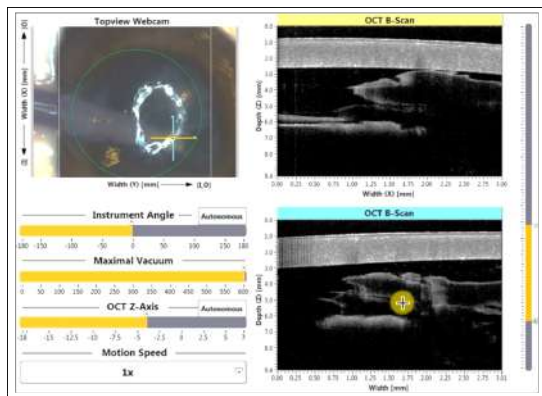

Fig. 13: The user interface for intraoperative intervention.

custom, real-time OCT scans can be acquired to provide timely information regarding the I/A tool and anatomical features.

Acknowledging the difficulty inherent to real-time image processing of OCT images, the user interface was designed to improve visualization and enable direct targeting of lens material (Fig. 13). The OCT probe can be translated to track the posterior capsule, lens material, or other features of interest. The frame rate of a B-scan (the time interval between each update without saving the data) is approximately 8 Hz and is limited by the motion bandwidth of the mechanical galvo mirror. The frame rate of a localized scan volume is approximately 1.5 Hz.

2) Intervention Strategy: Based on the real-time OCT feedback, several options are provided to the user.

(i) The user can offset and resize the workspace of the predefined trajectory. The trajectory $p(t)$ is modified according to the adjusted workspace:

$$p'(t) = RS\left[p(t) - c\right] + T + c \qquad (8)$$

where R and S are the rotation and scaling matrices representing the workspace deformation, T is the translation vector representing the workspace translation, and the iris center c is the resizing center. This function is critical in the event of eye deformation or corneal collapse because such events change the form of the anatomical structures from those at the beginning of the surgery.

(ii) The user can modify the tool-tip velocity or pause the motion while maintaining the aspiration.

(iii) The user can override the rotation angle of the surgical instrument. This function is used to create intraocular turbulence which is useful to detach large pieces of lens material from the posterior capsule.

(iv) The user can command the tool tip to any point inside the workspace by clicking on the displayed images. The camera view determines the (x, y) coordinates of the target while the z coordinate is assigned from localized OCT B-scans. This function can be used to target and remove floating lens material and air bubbles (see Supplemental Video 3). If a user requests a point outside the tool workspace or beyond the safety margins, a bisection algorithm determines the boundary point closest to the target (Algorithm 1) without formulating and solving a convex optimization problem. The tool tip will move towards the commanded point and then stop when its distance to the boundary is less than the threshold ϵ.

(v) The user can request emergency termination of the surgery. Once asked, the instrument will cease aspiration and begin to retract from the eye within 200 ms.

3) Intermittent Volume Scan Assessment: To assess surgical progress, evaluation is performed every two minutes by returning the tool to the standby position, pausing its motion, and acquiring an OCT volume scan (as demonstrated in Fig. 16). At this point, the surgeon can study the volume scan and inspect the eye. Based on this evaluation, one of

Algorithm 1 Algorithm for Rerouting Assigned Point

Inputs: Current position $\boldsymbol{p}_0$, assigned position $\boldsymbol{p}_{trg}$

Output: Feasible assigned point $\boldsymbol{p}^*$

Step 1: if $\boldsymbol{p}_{trg}$ is inside workspace, **return** $\boldsymbol{p}^* = \boldsymbol{p}_{trg}$

Step 2: $\Delta\boldsymbol{p} = \boldsymbol{p}_{trg} - \boldsymbol{p}_0$

    $(\alpha_{lb}, \alpha_{ub}) = (0, 1)$ and $\boldsymbol{p}^* = \boldsymbol{p}_0$

    do

        $\boldsymbol{p}_{prev} = \boldsymbol{p}^*$

        $\alpha = \frac{1}{2}(\alpha_{ub} - \alpha_{lb})$

        $\boldsymbol{p}^* = \boldsymbol{p}_0 + \alpha\Delta\boldsymbol{p}$

            if $\boldsymbol{p}^*$ is out of bounds, $\alpha_{ub} = \alpha$

            else $\alpha_{lb} = \alpha$

            end if

    while ($\left\|\boldsymbol{p}^* - \boldsymbol{p}_{prev}\right\|_2 > \epsilon$) or ($\boldsymbol{p}^*$ is out of bounds)

    return $\boldsymbol{p}^*$

---

three options can be chosen: (1) continuation of the cataract-extraction trajectory, (2) selection of specific points to target, or (3) termination of the surgery. Option (1) is useful if significant amounts of lens material remain in the anterior segment. Option (2) is useful for extracting small pieces of lens material. Option (3) is applied when no lens material appears in the OCT volume scans and the lens extraction is considered complete.

IV. EVALUATION AND ANIMAL MODEL TESTS

A. Engineering Evaluations

(1) Accuracy of OCT–IRISS Coordinate Frame Relationship: To test the accuracy of the OCT–IRISS coordinate frame relationship, the I/A tool was commanded to touch a series of $n = 30$ randomly generated points within its workspace. At each point, a volume scan was acquired, the tool-tip position was determined, and the ideal tool-tip position was calculated from forward kinematics. The coordinate frame transformation was used to transform the tool-tip positions determined by the OCT scan into the IRISS frame. Ideally, these points would perfectly overlap the points obtained from the forward kinematics with zero error; in reality, some error exists. This error was calculated as the 3D Euclidean distance between each pair of points. The statistical measures of the errors for a typical derivation of the coordinate transformation are shown in Table I.

TABLE I: Error of Typical Coordinate Transformation

Min.	Mean	RMS	Max.	Std.
0.047	0.19	0.21	0.34	0.077

* All values in units of mm

(2) Accuracy of OCT-based Anatomical Model: To evaluate the accuracy of the anatomical model, it was compared to human-labeled ground truths on $n = 10$ randomly sampled OCT images from nine different eyes. The accuracy of posterior capsule detection, with the worst image quality among all tissue, was 79.6 ± 23.3 μm (the 95% confidence interval around the average). This modeling error was considered
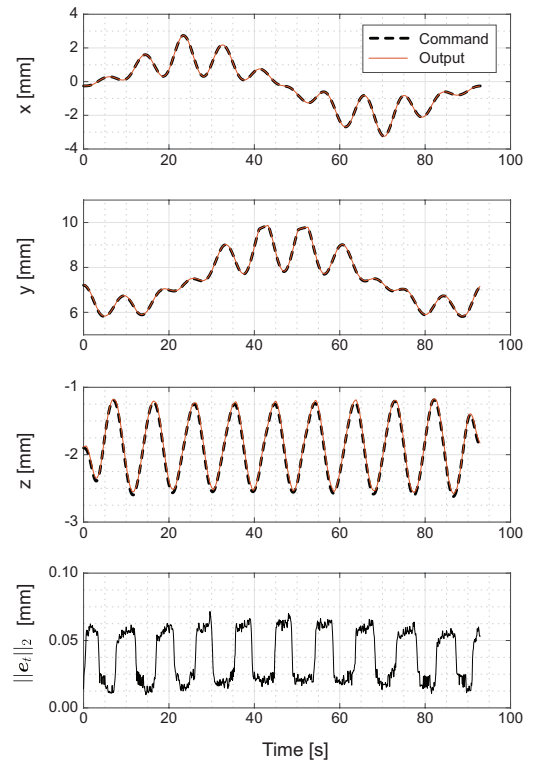

Fig. 14: Shown is the error in tip position along the trajectory where $\boldsymbol{e}_t$ is the tool-tip positional error.

negligible in comparison to the safety margins established near intraocular tissue, which are on the order of 1.5 mm.

(3) Accuracy of Cataract-Extraction Trajectory Tracking: The tracking performance of the IRISS along the predefined cataract-extraction trajectory was also evaluated by the positioning error $e_t(t)$:

$$\|\boldsymbol{e}_t(t)\|_2 = \|\boldsymbol{p}_{des}(t) - \boldsymbol{p}_{act}(t)\|_2 \tag{9}$$

where $\boldsymbol{p}_{des}(t)$ is the desired trajectory and $\boldsymbol{p}_{act}(t)$ is the actual tool-tip position measured from the optical encoder on each joint. In a typical trajectory tracking (Fig. 14), the maximum positioning error $e_t(t)$ is 71 μm, which is deemed negligible compared to the magnitude of the implemented safety margins (1.5 mm).

B. Animal Model Evaluations

The integrated system was tested in a clinical environment (Fig. 15). The animal model evaluation was performed on post-mortem pig eyes pinned in a Styrofoam holder. The objective was to autonomously remove the entire lens without posterior capsule rupture. The I/A hand-piece tool (92-IA21 Handle, Millennium Surgical) was mounted on the IRISS and fitted with a straight tip with side aspiration port (92-IA225). The tubing of the I/A tool was connected to the ACCURUS to provide irrigation and aspiration, the magnitude of which was controlled by the IRISS (Section II-C).

The automated OCT-guided lens extraction was performed and tested on $n = 30$ post-mortem pig eyes. For every eye, preoperative, intraoperative, and postoperative OCT volume scans were acquired for analysis. Microscope-based
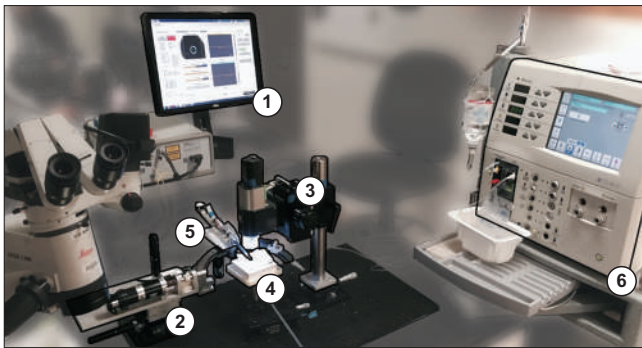
Fig. 15: Shown is the experimental setup for performing the animal model evaluation on post-mortem pig eyes. (1) User interface, (2) the IRISS, (3) OCT probe with integrated camera, (4) pig eye in fixture, (5) I/A tool in holder, and (6) the ACCURUS system.

examination was performed by a trained surgeon to assess the integrity of the tissues and to determine if lens material remained. The evaluation metrics include the volume of lens removed (0–100%) and whether posterior capsule rupture occurred (Y/N).

The surgical progress of an example surgery is shown in Fig. 16. After two minutes of tracking, a majority of lens remains in the anterior segment (Fig. 16a). The OCT volume scan indicates a second, deeper extraction cycle is required. After four minutes of tracking (Fig. 16b), most of the lens material has been removed and only a small piece of lens material remains attached to the posterior capsule. At this state, a third cycle would be less efficient than targeting the remaining piece; therefore, the I/A tool is commanded to this position and aspirates the remaining material. A postoperative OCT volume scan (Fig. 16c) reveals that no lens material remains in the anterior segment. Based on the convex shape of the posterior capsule, it is clear that the capsule remains intact.

In summary, posterior capsule rupture was avoided in all 30 trials. Complete lens extraction (100%) was achieved on 25 of the samples. In all five cases where 100% extraction was not achieved, minute particles of lens material were discovered post-surgery hidden behind or attached to the iris or posterior capsule where the OCT was unable to image. Therefore, the imperfect success rate was due to limitations of the sensing technology and we expect that with improved sensor feedback, such as ultrasound biometry or intraocular OCT, the completeness of lens extraction can be ensured.

V. CONCLUSION

To reduce common complications in cataract surgery such as posterior capsule rupture, incomplete lens removal, and corneal incision leakage, an OCT-guided robotic system was developed for automated cataract extraction. Using OCT scan data, both preoperative planning and intraoperative intervention for the robotic system—the IRISS—was demonstrated. Automated alignment of the mechanical RCM to the corneal incision and an insertion trajectory were generated using image-based techniques. The eye anatomy was segmented through parametric modeling, within which a flower-shaped
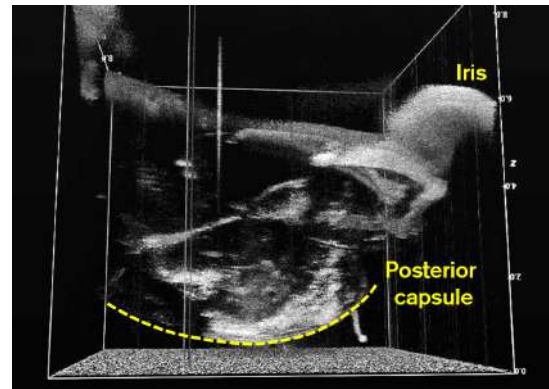
(a) After two minutes of operation, an intermittent volume scan reveals an intact posterior capsule and a majority of lens material remaining.
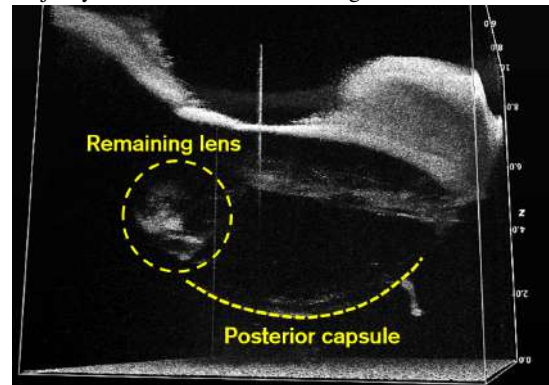
(b) After four minutes of operation, only a small piece of lens material remains.
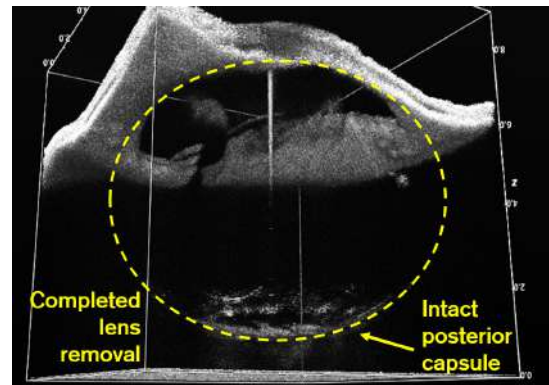
(c) This postoperative volume scan shows an intact posterior capsule and complete removal of lens removal.

Fig. 16: Shown are three examples of OCT volume scans for intraoperative and postoperative evaulation.

trajectory was generated to aspirate lens material while preserving a safety margin with anatomical bounds.

To account for the changing surgical environment, various strategies for monitoring and intervening in the autonomous cataract extraction were adopted. For example, the surgeon can override the robot motion and assign a specific target for the tool tip. The proposed strategy for intraoperative targeting was validated by aspirating an air bubble from the anterior chamber. In addition, the surgical progress can be monitored

by intermittent OCT volume scans.

A series of engineering measures demonstrated that the OCT-guided system has sufficient capability to perform automated cataract extraction: the coordinate transformation between OCT and IRISS exhibited 0.19±0.03 mm accuracy, the parametric anatomical model exhibited 79.6±23.3 μm accuracy, and tool-tip positional tracking exhibited a maximum error of 71 μm. The automated cataract-extraction procedure was tested on 30 post-mortem pig eyes. Only in five cases did the system leave small particles of lens material due to the inability of the OCT to sense them. In addition, there was no posterior capsule rupture among all 30 eyes tested.

The preclinical evaluation on post-mortem pig eyes is the first step to validate the effectiveness of the proposed robotic system for semi-automated lens extraction. Before further evaluations are performed on a live animal model or on a cadaveric/live human eye, several limitations of the current system must be properly addressed. First, the safety of the system requires rigorous testing and validation. Because intraoperative OCT images provide improved visualization of the posterior capsule, the proposed image-guided intervention is expected to be safer than manual operation under a microscope. Second, an eye tracking algorithm is required to detect the eye motion in actual practice. The XYZ stage can be commanded to maintain the alignment between the RCM and the surgical incision. To limit the eyeball movement, we also propose a suction-based fixation device. Third, the learning curve of the proposed intervention requires further analysis. The average surgical duration of the preclinical evaluation was 277 s. Although this is faster than the robot-assisted teleoperation we performed (331–487 s [34]), we believe there is room for improvement.

Furthermore, an OCT-based tissue-detection algorithm is desirable to facilitate the automation of intraoperative intervention. The information should be used to update the workspace and adjust the navigation strategy to prevent tissue damage and improve surgical efficacy. Also, an alternative strategy to image behind the iris could improve the success rate of lens material removal.

Author Contribution

Chen performed the system integration, software design, OCT image segmentation and anatomy modeling, and intervention interface; Lee performed the software design, cataract-extraction trajectory generation, and implementation of rerouting algorithm; Gerber performed the hardware design for OCT stage motorization, automated OCT registration, tool alignment, insertion, and digital ACCU-RUS control; Cheng analyzed the requirements and set up the OCT imaging system; Yang evaluated the OCT image segmentation algorithm; Govetto and Francone performed animal model evaluations with Chen, Lee, and Gerber; Soatto offered insights on OCT image processing; Grundfest contributed in asserting the requirements of the OCT imaging system; Hubschman contributed in asserting the surgical requirements, approving the conceptual design. He also led animal model evaluation, the clinical aspect of the development, and co-led the project team with Tsao; and Tsao conceived the IRISS, performed the conceptual design, led the engineering aspect of the development, and co-led the project team with Hubschman. The manuscript was written by Chen, Lee, Gerber, and Tsao.

References

[1] D. Pascolini and S. P. Mariotti, "Global estimates of visual impairment: 2010," *British J. of Ophthalmology*, vol. 96, no. 5, pp. 614–618, 2012.

[2] R. J. Olson, R. Braga-Mele, S. H. Chen, K. M. Miller, R. Pineda, J. P. Tweeten, and D. C. Musch, "Cataract in the adult eye preferred practice pattern®," *Ophthalmology*, vol. 124, no. 2, pp. 1–119, 2017.

[3] National Eye Institute. Facts About Cataract. Last accessed: 11/16/2017. [Online]. Available: https://nei.nih.gov/health/cataract/cataract_facts

[4] P. Desai, D. Minassian, and A. Reidy, "National cataract surgery survey 1997–8: a report of the results of the clinical outcomes," *British J. of Ophthalmology*, vol. 83, no. 12, pp. 1336–1340, 1999.

[5] L. Fanea and A. J. Fagan, "Magnetic resonance imaging techniques in ophthalmology," *Molecular vision*, vol. 18, p. 2538, 2012.

[6] R. H. Silverman, "High-resolution ultrasound imaging of the eye–a review," *Clinical & experimental ophthalmology*, vol. 37, no. 1, pp. 54–67, 2009.

[7] J. Fujimoto and E. Swanson, "The development, commercialization, and impact of optical coherence tomographyhistory of optical coherence tomography," *Investigative ophthalmology & visual science*, vol. 57, no. 9, pp. OCT1–OCT13, 2016.

[8] O. M. Carrasco-Zevallos, C. Viehland, B. Keller, M. Draelos, A. N. Kuo, C. A. Toth, and J. A. Izatt, "Review of intraoperative optical coherence tomography: technology and applications," *Biomedical Optics Express*, vol. 8, no. 3, pp. 1607–1637, 2017.

[9] S. Radhakrishnan, A. M. Rollins, J. E. Roth, S. Yazdanfar, V. Westphal, D. S. Bardenstein, and J. A. Izatt, "Real-time optical coherence tomography of the anterior segment at 1310 nm," *Archives of ophthalmology*, vol. 119, no. 8, pp. 1179–1185, 2001.

[10] M. Esmaeelpour, B. Považay, B. Hermann, B. Hofer, V. Kajic, K. Kapoor, N. J. Sheen, R. V. North, and W. Drexler, "Three-dimensional 1060-nm oct: choroidal thickness maps in normal subjects and improved posterior segment visualization in cataract patients," *Investigative ophthalmology & visual science*, vol. 51, no. 10, pp. 5260–5266, 2010.

[11] K. E. Donaldson, R. Braga-Mele, F. Cabot, R. Davidson, D. K. Dhaliwal, R. Hamilton, M. Jackson, L. Patterson, K. Stonecipher, S. H. Yoo *et al.*, "Femtosecond laser–assisted cataract surgery," *J. of Cataract & Refractive Surgery*, vol. 39, no. 11, pp. 1753–1763, 2013.

[12] D. Palanker, G. Schuele, N. Friedman, D. Andersen, and W. Culbertson, "Cataract surgery with oct-guided femtosecond laser," in *Bio-Optics: Design and Application*. Optical Society of America, 2011, p. BTuC4.

[13] Abbott Medical Optics. CATALYS Precision Laser System. Last accessed: 10/17/2016. [Online]. Available: http://www.optimedica.com/catalysoverview

[14] LENSAR, LLC. The LENSAR Laser System. Last accessed: 10/17/2016. [Online]. Available: http://www.lensar.com/system.php

[15] Alcon. LenSx Laser. Last accessed: 10/17/2016. [Online]. Available: https://www.myalcon.com/products/surgical/lensx-laser/index.shtml

[16] D. Allen, M. Habib, and D. Steel, "Final incision size after implantation of a hydrophobic acrylic aspheric intraocular lens: new motorized injector versus standard manual injector," *J. of Cataract & Refractive Surgery*, vol. 38, no. 2, pp. 249–255, 2012.

[17] A. Üneri, M. A. Balicki, J. Handa, P. Gehlbach, R. H. Taylor, and I. Iordachita, "New steady-hand eye robot with micro-force sensing for vitreoretinal surgery," in *Biomedical Robotics and Biomechatronics (BioRob), 2010 3rd IEEE RAS and EMBS International conf. on.* IEEE, 2010, pp. 814–819.

[18] T. Ueta, Y. Yamaguchi, Y. Shirakawa, T. Nakano, R. Ideta, Y. Noda, A. Morita, R. Mochizuki, N. Sugita, M. Mitsuishi *et al.*, "Robot-assisted vitreoretinal surgery: Development of a prototype and feasibility studies in an animal model," *Ophthalmology*, vol. 116, no. 8, pp. 1538–1543, 2009.

[19] S. Tanaka, K. Harada, Y. Ida, K. Tomita, I. Kato, F. Arai, T. Ueta, Y. Noda, N. Sugita, and M. Mitsuishi, "Quantitative assessment of manual and robotic microcannulation for eye surgery using new eye model," *The International J. of Medical Robotics and Computer Assisted Surgery*, vol. 11, no. 2, pp. 210–217, 2015.

[20] H. Yu, J.-H. Shen, K. M. Joos, and N. Simaan, "Design, calibration and preliminary testing of a robotic telemanipulator for oct guided retinal surgery," in *Robotics and Automation (ICRA), 2013 IEEE International conf. on*. IEEE, 2013, pp. 225–231.

[21] M. Nambi, P. S. Bernstein, and J. J. Abbott, "A compact retinal-surgery telemanipulator that uses disposable instruments," in *International conf. on Medical Image Computing and Computer-Assisted Intervention*. Springer, 2015, pp. 258–265.

[22] M. Nasseri, M. Maier, and C. Lohmann, "A targeted drug delivery platform for assisting retinal surgeons for treating age-related macular degeneration (amd)," in *Engineering in Medicine and Biology Society (EMBC), 2017 39th Annual International conf. of the IEEE*. IEEE, 2017, pp. 4333–4338.

[23] J. T. Wilson, M. J. Gerber, S. W. Prince, C.-W. Chen, S. D. Schwartz, J.-P. Hubschman, and T.-C. Tsao, "Intraocular robotic interventional surgical system (iriss): Mechanical design, evaluation, and master–slave manipulation," *The International J. of Medical Robotics and Computer Assisted Surgery*, 2017.

[24] J. P. Ehlers, S. K. Srivastava, D. Feiler, A. I. Noonan, A. M. Rollins, and Y. K. Tao, "Integrative advances for oct-guided ophthalmic surgery and intraoperative oct: microscope integration, surgical instrumentation, and heads-up display surgeon feedback," *PLoS One*, vol. 9, no. 8, p. e105224, 2014.

[25] M. T. El-Haddad and Y. K. Tao, "Automated stereo vision instrument tracking for intraoperative oct guided anterior segment ophthalmic surgical maneuvers," *Biomedical optics express*, vol. 6, no. 8, pp. 3014–3031, 2015.

[26] H. Yu, J.-H. Shen, R. J. Shah, N. Simaan, and K. M. Joos, "Evaluation of microsurgical tasks with oct-guided and/or robot-assisted ophthalmic forceps," *Biomedical optics express*, vol. 6, no. 2, pp. 457–472, 2015.

[27] H. Yu, J.-H. Shen, K. M. Joos, and N. Simaan, "Calibration and integration of b-mode optical coherence tomography for assistive control in robotic microsurgery," *IEEE/ASME Trans. on Mechatronics*, vol. 21, no. 6, pp. 2613–2623, 2016.

[28] G. W. Cheon, Y. Huang, J. Cha, P. L. Gehlbach, and J. U. Kang, "Accurate real-time depth control for cp-ssoct distal sensor based handheld microsurgery tools," *Biomedical optics express*, vol. 6, no. 5, pp. 1942–1953, 2015.

[29] G. W. Cheon, B. Gonec, R. H. Taylor, P. L. Gehlbach, and J. U. Kang, "Motorized micro-forceps with active motion guidance based on common-path ssoct for epiretinal membranectomy," *IEEE/ASME Trans. on Mechatronics*, 2017.

[30] Alcon. ACCURUS® Surgical System. Last accessed: 11/16/2017. [Online]. Available: https://www.myalcon.com/products/surgical/docs/Accurus_2-12.pdf

[31] I. Sanchez, R. Martin, F. Ussa, and I. Fernandez-Bueno, "The parameters of the porcine eyeball," *Graefe's Archive for Clinical and Experimental Ophthalmology*, vol. 249, no. 4, pp. 475–482, 2011.

[32] J. C. Gower and G. B. Dijksterhuis, *Procrustes problems*. Oxford University Press on Demand, 2004, vol. 30.

[33] D. Williams, Y. Zheng, F. Bao, and A. Elsheikh, "Automatic segmentation of anterior segment optical coherence tomography images." *J. of biomedical optics*, vol. 18, no. 5, pp. 056 003–056 003, 2013.

[34] E. Rahimy, J. Wilson, T. Tsao, S. Schwartz, and J. Hubschman, "Robot-assisted intraocular surgery: development of the iriss and feasibility studies in an animal model," *Eye*, vol. 27, no. 8, p. 972, 2013.